



Automated diagnosis of focal liver lesions using bidirectional empirical mode decomposition features



U. Rajendra Acharya^{a,b,c,*}, Joel En Wei Koh^a, Yuki Hagiwara^a, Jen Hong Tan^a,
Arkadiusz Gertych^d, Anushya Vijayanathan^e, Nur Adura Yaakup^e, Basri Johan Jeet Abdullah^e,
Mohd Kamil Bin Mohd Fabell^e, Chai Hong Yeong^{e,f}

^a Department of Electronics and Computer Engineering, Ngee Ann Polytechnic, Singapore

^b Department of Biomedical Engineering, School of Science and Technology, Singapore University of Social Sciences, Singapore

^c Department of Biomedical Engineering, Faculty of Engineering, University of Malaya, Malaysia

^d Department of Surgery, Department of Pathology and Laboratory Medicine, Cedars-Sinai Medical Center, Los Angeles, CA, USA

^e Department of Biomedical Imaging, Faculty of Medicine, University of Malaya, Kuala Lumpur, Malaysia

^f School of Medicine, Faculty of Health and Medical Sciences, Taylor's University, Malaysia

ARTICLE INFO

Keywords:

Computer-aided diagnostic system

Liver lesions

Benign

Malignant

Machine learning

Ultrasonography

ABSTRACT

Liver is the heaviest internal organ of the human body and performs many vital functions. Prolonged cirrhosis and fatty liver disease may lead to the formation of benign or malignant lesions in this organ, and an early and reliable evaluation of these conditions can improve treatment outcomes. Ultrasound imaging is a safe, non-invasive, and cost-effective way of diagnosing liver lesions. However, this technique has limited performance in determining the nature of the lesions. This study initiates a computer-aided diagnosis (CAD) system to aid radiologists in an objective and more reliable interpretation of ultrasound images of liver lesions. In this work, we have employed radon transform and bi-directional empirical mode decomposition (BEMD) to extract features from the focal liver lesions. After which, the extracted features were subjected to particle swarm optimization (PSO) technique for the selection of a set of optimized features for classification. Our automated CAD system can differentiate normal, malignant, and benign liver lesions using machine learning algorithms. It was trained using 78 normal, 26 benign and 36 malignant focal lesions of the liver. The accuracy, sensitivity, and specificity of lesion classification were 92.95%, 90.80%, and 97.44%, respectively. The proposed CAD system is fully automatic as no segmentation of region-of-interest (ROI) is required.

1. Introduction

Liver is the largest internal organ in the body. It neutralizes toxins, assists in the processing of proteins and fats from digested food, keeps important nutrients, and produces and secretes bile [1,2].

According to the American Cancer Society, liver cancer is the 8th leading cause of cancer related death in women and 5th in men worldwide [3]. The death rates due to liver cancer have tripled since the year 2000. One of the reasons is the lack of tools to detect early symptoms of the disease [4], and hence many patients are diagnosed with liver cancer in an advanced stage. Lesions of the liver are often found by chance during a routine check-up with ultrasound examination [5]. Thus, differentiating the lesion type at the time of diagnosis can be beneficial to the patients. Focal liver lesions can either be benign (non-cancerous) or

malignant (cancerous). Examples of benign lesions are liver cysts, liver abscesses, hemangioma, focal nodular hyperplasia, and hepatic adenoma [6]. Malignant lesions are hepatocellular carcinoma (HCC), cholangiocarcinoma, biliary cystadenocarcinoma, and lesions from metastases (MET) originating from cancers in other organs [6]. Preexisting conditions such as fatty liver disease and cirrhosis can increase the risk of developing a liver cancer [7].

Histopathological examination (HPE) of a biopsy sample is the gold standard to characterize a liver lesion. However, biopsy is an invasive and costly surgical procedure. Ultrasound imaging has been used as a common diagnostic tool for initial diagnosis of the liver because it is non-invasive, non-ionizing and cost-effective. However, it is difficult for radiologists to determine the nature of the lesion based on the images alone. To overcome this shortcoming, we developed a computer-aided

* Corresponding author. Department of Electronics and Computer Engineering, Ngee Ann Polytechnic, 599489, Singapore.
E-mail address: aru@np.edu.sg (U.R. Acharya).

diagnosis (CAD) system to aid in the characterization of liver lesion using ultrasound images.

The literature review on the development of CAD systems to discriminate between the different liver lesions is scarce (see Table 1). Aside these papers, there are also CAD systems developed for fatty liver disease and cirrhosis [8]. Acharya et al. [9–12] investigated multiple techniques to develop a robust algorithm to assist in the early diagnosis of liver diseases such as fatty liver disease and cirrhosis. Having a CAD system to detect liver lesions at an early stage could be helpful in identifying the severity of the lesions, including cancer at earliest possible time [8].

Several authors have used contrast-enhanced ultrasound (CEUS) images for the identification of focal liver lesions [13–15]. A few CAD systems were also developed using CEUS images. Sugimoto et al. [16] and Shiraishi et al. [17] used CEUS images for the automated identification of focal liver lesions.

In this work, we proposed to develop an automated CAD system for the classification of liver lesions into normal, benign, and malignant classes using conventional ultrasound images. CEUS images were not considered in this work as the examination is invasive and involves additional costs to the patients. In most countries, CEUS is performed as the second-line imaging method after inconclusive baseline ultrasound for the diagnosis of benign focal liver lesions [18]. Fig. 1 illustrates the different types of focal liver lesions included in this study.

2. Data collection

This study was approved by the Medical Research Ethics Committee, University of Malaya Medical Centre, Malaysia (Protocol No. MEC 937.13). The liver ultrasound images and HPE results were retrieved retrospectively from the Radiological Information System and Electronic Medical Record system of the Department of Biomedical Imaging, University of Malaya Medical Centre, Kuala Lumpur, Malaysia. The data were collected for a period of 3 years, from the year 2014–2017, and

included 463 ultrasound images from 101 patients (86 males, 15 females, aged 58.5 ± 15.1 years) to develop the CAD tool. Ultrasound imaging findings were validated with biopsies. Table 2 shows the total number of images (78 normal, 26 benign, and 36 malignant) used in each class.

3. Methodology

A graphical representation of the proposed technique is reflected in Fig. 2.

3.1. Pre-processing

The ultrasound images (256×256 pixels) were subjected to contrast limited adaptive histogram equalization (CLAHE) [25]. CLAHE works by enhancing to small tiles (8×8 pixels) and bilinear interpolation is used to combine neighboring tiles to remove boundaries, resulting in equalize intensity and improve contrast [26].

Subsequently, Radon transform and Top-hat filtering were applied.

3.2. Features extraction

The Bi-dimensional empirical mode decomposition (BEMD) [27] is then executed to extract features from the top-hat transformed liver images. BEMD is the 2-D extension of the empirical mode decomposition, which uses a sifting process which considers the neighbouring windows to detect extrema iteratively [28]. The sifting process uses radial basis function to connect the maxima and minima points, forming an ‘envelope’.

The local mean is found by averaging 2 envelopes and deducted from the liver image to find the first intrinsic mode functions (IMF), and the process is repeated to extract other IMFs. The riding waves (oscillations with no zero-crossing between extrema) are removed, and uneven amplitude are smoothed by the sifting process.

The BEMD [29] extracts a 2-D finite number of oscillatory

Table 1
Selected published studies on the CAD system for focal liver lesions.

Authors, Year	Number of Images	Methodology		Segmentation of ROI	Performance (%)		
		Features	Classifier Used		Acc	Sen	Spec
Mittal et al. [19], 2011	N: 16 C: 17 H: 18 HCC: 15 MET: 45	• Textural	• NN	Yes	86.40	–	–
Virmani et al. [20], 2013a	HCC: 27 MET: 27	• Textural • GA-SVM	• SVM	Yes	91.60	–	–
Virmani et al. [21], 2013b	N: 21 C: 12 H: 15 HCC: 28 MET: 32	• Textural • PCA	• SVM	Yes	87.20	–	–
Virmani et al. [22], 2014	N: 21 C: 12 H: 15 HCC: 28 MET: 32	• Textural • PCA	• NNE	Yes	95.00	–	–
Hwang et al. [23], 2015	C: 29 H: 37 M: 33	• Textural • PCA	• ANN	Yes	<96.00	–	–
Manth et al. [24], 2016	H: 16 HCC: 28	• Textural	• SSVM	Yes	94.30	–	–
Present study	N: 78 B: 26 M: 36	• Radon transform • Top-Hat • Bi-EMD • ADASYN • PSO	• PNN	No (Fully-automated)	92.95	90.80	97.44

ROI = region of interest, Acc = accuracy, Sen = sensitivity, Spec = specificity, B = benign, C = cyst, H = hemangioma, HCC = hepatocellular carcinoma, M = malignant, MET = metastases, N = normal, GA-SVM = genetic algorithm-support vector machine, PCA = principal component analysis, ANN = artificial neural network, NN = neural network, NNE = neural network ensemble, SVM = support vector machine, SSVM = smooth support vector machine.



Fig. 1. The different types of focal liver lesions.

Table 2
The number of ultrasound images used in normal, benign, and malignant classes.

	Normal	Benign			Malignant	
		Abscess	Cysts	Haemangioma	HCC	MET
	78	5	17	4	26	10
Total	78	26			36	

components also known as IMF into different scales. 3 x IMFs (Imf_1^{coeff} , Imf_2^{coeff} , and Imf_3^{coeff}) and 1 x residue (res) were obtained from the BEMD decomposition. The Imf_x^{coeff} is the scale of the IMF component where x represents level 1, 2, or 3, and *coeff* denotes the coefficient of the IMF component. Subsequently, the DCT coefficients [30] were extracted from the IMFs and residue to obtain more distinctive features for the classification of the three classes. Fig. 3 shows the output (Radon transform, Top-hat, DCT coefficient, and BEMD) of normal, benign, and malignant liver lesion images. The 2-D DCT coefficients were then converted to a 1-D feature vector by concatenating rows of the 2-D DCT [31].

3.3. Features reduction

A total of 264,240 features were extracted from the DCT coefficients. Due to the massive number of extracted features, the features are reduced, and only statistically significant features are retained. Hence, an analysis of variance (ANOVA) is carried out to reduce the size of the feature set. Next, an adaptive synthetic sampling approach (ADASYN) is executed to make up for the unbalance class distribution. Then, of the particle swarm optimization (PSO) is applied to choose 30 optimum features for classification.

The ANOVA [32] is a statistical test that computes the differences and their variation among the three classes (normal, benign, and malignant). The p-value and F-value parameters are used to determine the significance of the features. The p-value and F-value are inversely related. A low p-value (<0.001) indicates statistical significance and a high F-value indicates that the feature is indicative of the large difference among features subjected to the test [32]. After the ANOVA test, a total of 14,460 significant features were selected.

The ADASYN [33] generates synthetic data samples from the extracted data to ensure that the number of samples is proportionately distributed in each class. After applying ADASYN, the number of samples of the normal, benign, and malignant class is 78, 78, and 85 respectively (refer to Table 2 for the number of samples before ADASYN). The main purpose of introducing ADASYN in this work is to reduce the learning biases instilled during the training process by producing synthetic data to balance out the sample data in the three classes. The algorithm starts off by computing the degree of imbalances among the three classes. Then, it determines the number of data samples required in the minority classes. The parameters are set to Euclidean distance with a neighbor k = 5.

The PSO [34] is a swarm-based optimizer approach that is performed to select a set of features required for optimal diagnostic performance when fed into the classifier. The PSO mimics the conduct of a flock of birds hunting for food within a compound. The birds start off with zero knowledge of the food whereabouts. However, they gain confidence in their knowledge of the food location after every round of hunt. Hence, this is an optimizer technique whereby the PSO searches for the best route (features) to correctly identify the normal, benign, and malignant classes. A subset of features was randomly chosen and fed into a classifier wrapped in the PSO and optimized using misclassification error iteratively. A total of 30 features were selected by the PSO. The PSO

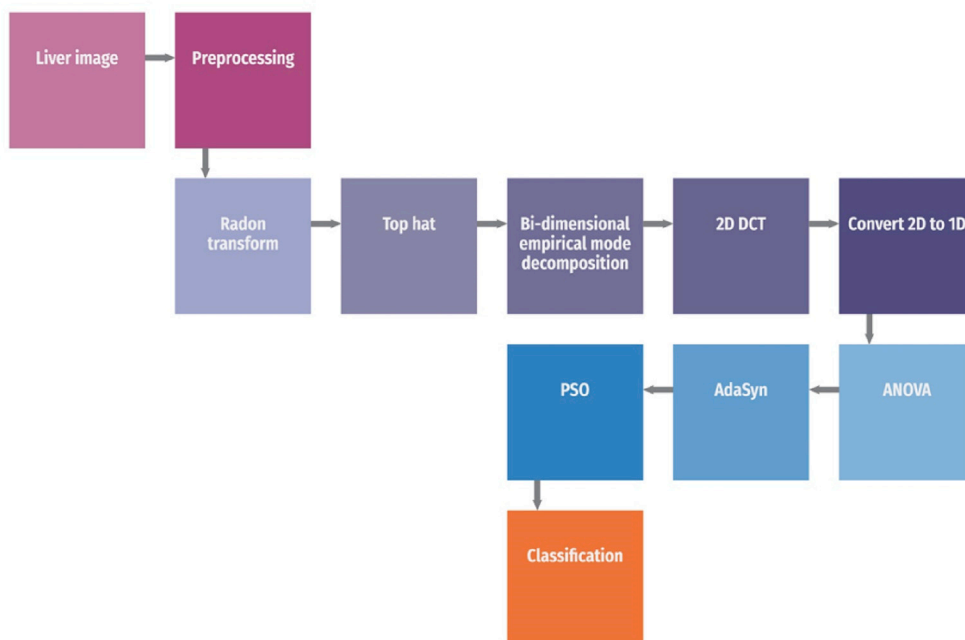


Fig. 2. The proposed methodology to develop the CAD system.

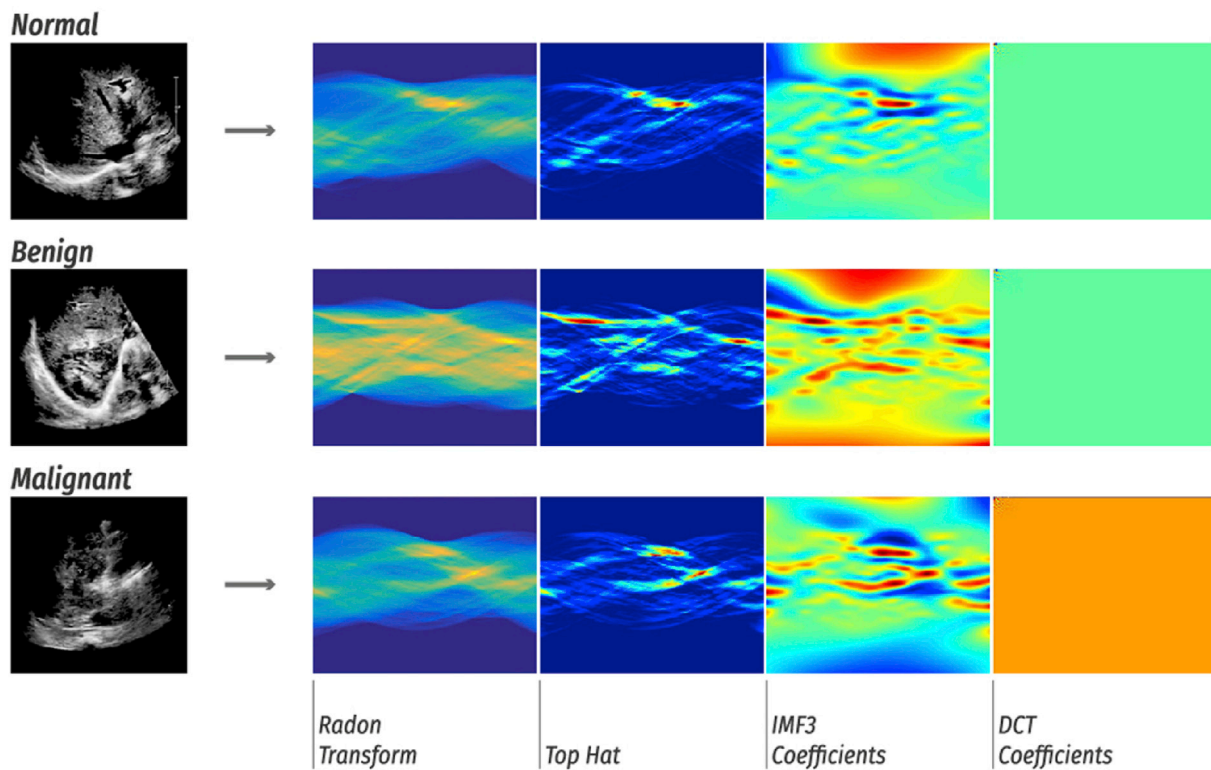


Fig. 3. Sample of outputs of normal, benign, and malignant liver lesions.

parameters used in this work are set at $w = 0.730$, $c1 = 1.496$, and $c2 = 1.496$ where w , $c1$, and $c2$ represent inertia weight, personal learning coefficient, and global learning coefficient respectively.

3.4. Classification

A few classifiers namely the probabilistic neural network (PNN) [35] with a spread of 0.03, support vector machine (SVM) with a sigma of 2.3 [36], linear discriminant analysis (DL) [37], k-nearest neighbor (kNN) with $k = 5$ [38], and random forest (RF) with 100 trees and a minimum leaf size of 1 [39] are applied in this work to classify the liver images into normal, benign, and malignant class. A ten-fold cross-validation [40] technique is implemented in this study. The performance of the proposed system is based on the accuracy, sensitivity, and specificity yielded using the test data. The receiver operating characteristic (ROC) curve is also plotted to validate the effectiveness of the proposed system.

4. Results

The proposed algorithm was developed in the MATLAB environment and trained on a workstation with an Intel i7-4770, 3.47 GHz Haswell Processor using Microsoft Window 10, 16 GB, 1600 MHz, CL9 DDR3-RAM.

Fig. 4 (a) and (b) are representations of the selected features (total of 30 features) from the three classes after performing PSO (refer to Table A1). Furthermore, specificity, sensitivity, and accuracy yielded for the model trained with 2–30 features are recorded in Table 3. It is observed that the diagnostic accuracy of the proposed algorithm increases with increasing number of features. The best accuracy (92.95%) is achieved with 29 features. This proposed technique yielded a maximum sensitivity and specificity of 90.80% and 97.44% respectively in the discrimination of the three classes.

Furthermore, the ROC curves are plotted with the sensitivity against

the specificity as shown in Fig. 5. It can be noted that a high area under curve (AUC) value of 0.941 is obtained for PNN classifier. Furthermore, few classifiers namely the DL, kNN, RF, and SVM were employed to validate the proposed algorithm. High AUC values are seen for all the classifiers in Fig. 5 and therefore our proposed system is reliable. In this study, the benign and malignant classes are treated as one (abnormal) class and normal as another class. Hence it is a two-class problem for ROC.

Table 4 records the average time needed to pre-process the ultrasound liver images, to extract the features, and the time taken to identify the liver images. It is noted that only approximately 23 s are needed for the proposed system to diagnosis the liver images.

5. Discussion

Based on the output after applying radon transform and Top-hat in Fig. 3, it is observed that the imf_3 coefficients extracted from each class are distinct. Hence, this shows that the proposed technique (radon transform and BEMD) can capture minute variations in the different liver images and are able to classify these images accordingly.

Table 1 shows a summary of selected works in the development of CAD system to automatically classify the different liver lesions (benign or malignant) using ultrasound images. Mittal et al. [19] developed an algorithm to differentiate normal, benign (i.e. hemangioma and cysts), and malignant (i.e. HCC and metastasis) lesions. They extracted textural features from the images and fed them to the neural network classifier which yielded an accuracy of 86.40%. Likewise, in the works by Virmani et al. [20–22], they extracted textural features from the 5 classes of liver images. An accuracy of 91.60% [20], 87.20% [21], and 95.00% [22] was achieved using SVM classifier [20,21], and neural network ensemble classifier [22] respectively.

Hwang et al. [23] employed different textural feature extraction techniques to pick up characteristic features to identify the focal liver

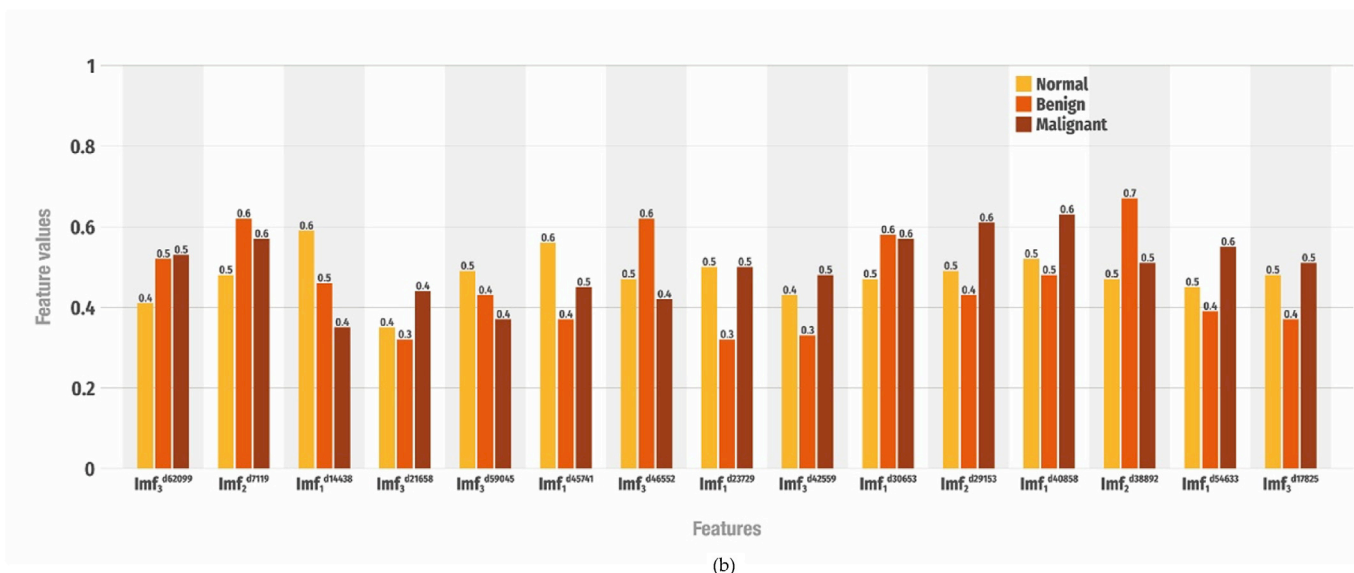
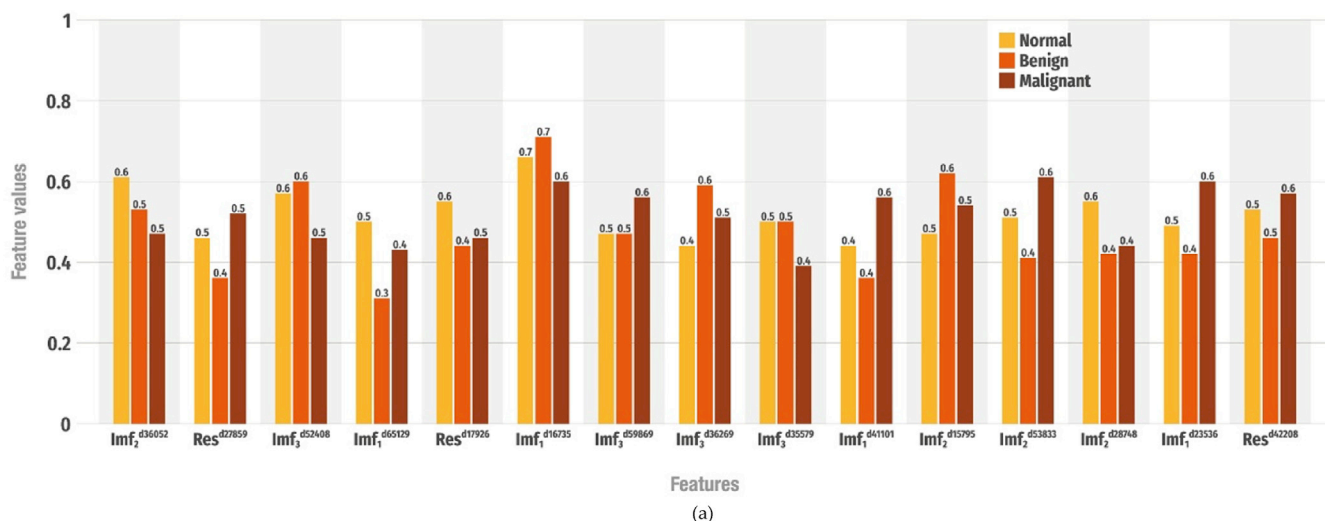


Fig. 4. The bar plot of selected features extracted from the three classes.

lesions. These features were reduced by PCA technique and fed to the ANN classifier. Their proposed method has shown a high diagnostic accuracy of more than 96.00%.

Manth et al. [24] developed a system to automatically distinguish between benign (i.e. hemangioma) and malignant (HCC) liver lesions. They have extracted textural features from 16 hemangioma and 28 HCC liver lesions and obtained an accuracy of 94.30%.

Even though the proposed technique did not achieve the highest performance in terms of accuracy, specificity, and sensitivity, it should be noted that the works recorded in Table 1 required segmentation of the region-of-interest (ROI) before extracting significant features for classification. Nevertheless, our proposed approach is fully-automated, and no segmentation of ROI is required. Furthermore, we have implemented all the existing techniques from the literature and found that our proposed method obtained the highest diagnostic performance using our images.

The ultrasound liver images were only enhanced with CLAHE whereas, in the works recorded in Table 1, the ROI was segmented in the pre-processing step. This shows that the proposed method is robust as

this methodology can identify the liver lesion and extract distinctive features without segmentation process. Nonetheless, the algorithm can be improved by having a bigger data samples to train the performance of the classifier.

The recorded studies have used textural features to classify the lesions accordingly. In this work, we also employed a textual-based features extraction technique to extract indicative features for classification. In addition, ADASYN was introduced to balance the sample data in the 3 classes to ensure that no biases were introduced during the training phase. Moreover, an optimization technique was applied to select a group of features that will complement with one another to produce optimal classification performance.

A 3-class classification problem was initiated in this work as the number of images acquired in each benign and malignant class was relatively small. Thus, the different abnormalities which are a cluster of the benign class are combined into one class and the different cancerous lesions such as the HCC and metastasis are grouped into the malignant class. Nevertheless, we would like to expand this work into a 5-class

Table 3
The performance measures obtained using different number of features with the PNN classifier.

No. Of F.	TP	TN	FP	FN	Performances in %			
					Accuracy	PPV	Sensitivity	Specificity
2	103	33	45	60	56.43	69.59	63.19	42.31
3	120	24	54	43	59.75	68.97	73.62	30.77
4	122	39	39	41	66.80	75.78	74.85	50.00
5	137	31	47	26	69.71	74.46	84.05	39.74
6	142	35	43	21	73.44	76.76	87.12	44.87
7	135	52	26	28	77.59	83.85	82.82	66.67
8	131	62	16	32	80.08	89.12	80.39	79.49
9	127	71	7	36	82.16	94.78	77.91	91.03
10	124	74	4	39	82.16	96.88	76.07	94.87
11	119	75	3	44	80.50	97.54	73.01	96.15
12	147	48	30	16	80.91	83.05	90.18	61.54
13	148	60	18	15	86.31	89.16	90.80	76.92
14	147	64	14	16	87.55	91.30	90.18	82.05
15	146	66	12	17	87.97	92.41	89.57	84.62
16	141	68	10	22	86.72	93.38	86.50	87.18
17	142	72	6	21	88.80	95.95	87.12	92.31
18	141	75	3	22	89.63	97.92	86.50	96.15
19	139	77	1	24	89.63	99.29	85.28	98.72
20	137	77	1	26	88.80	99.28	84.05	98.72
21	137	78	0	26	89.21	100.00	84.05	100.00
22	135	78	0	28	88.38	100.00	82.82	100.00
23	148	67	11	15	89.21	93.08	90.80	85.90
24	148	66	12	15	88.80	92.50	90.80	84.62
25	148	69	9	15	90.04	94.27	90.80	88.46
26	148	70	8	15	90.46	94.87	90.80	89.74
27	148	73	5	15	91.70	96.73	90.80	93.59
28	148	73	5	15	91.70	96.73	90.80	93.59
29	148	76	2	15	92.95	98.67	90.80	97.44
30	146	77	1	17	92.53	99.32	89.57	98.72

No. Of F. = number of features, TP = true positive, TN = true negative, FP = false positive, FN = false positive, PPV = positive predictive value. The bold words signify that the results obtained are the best.

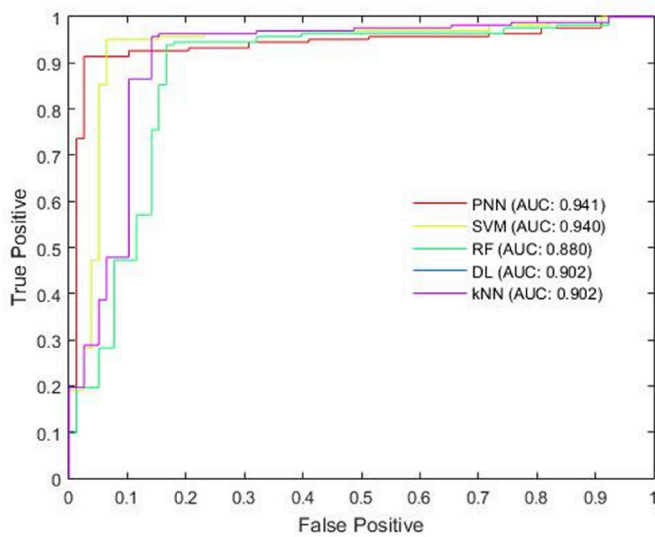


Fig. 5. The ROC plot for different classifiers.

classification problem to characterize the different types of benign and malignant lesions in future work. This requires a larger number of ultrasound images with varying types of liver lesions.

In addition, with more images collected for the next research work

Table 4
The average time performance for the proposed system.

Time taken in each step:	Time taken (seconds)
Pre-process	0.073
Radon transform	0.063
Top-hat	0.015
BEMD	22.696
DCT	0.037
Classification	0.008
Total time was taken	23

deep convolutional neural network (CNN) method would be preferred to automatically classify the ultrasound liver images into their respective classes [41,42]. Currently, the number of images is limited and a 5-class deep-learning based classifier is not recommended.

6. Conclusion

A fully automated liver lesions detection system is proposed in this work to assist radiologists in a reliable diagnosis of liver lesions. Given the good diagnostic accuracy obtained without any segmentation of ROI, this system has the potential to be utilized in clinics and hospitals to serve as a supporting tool in the evaluation of liver lesions in almost real-time. Hence, it will reduce the workload of the radiologists as they do not need to manually segment the ROI. Further, the proposed algorithm can also be extended to identify the different stages of liver fibrosis.

Appendix

Table A1
The statistics (mean and standard deviation) of selected features for normal, benign, and malignant liver lesion classes.

Features	Normal		Benign		Malignant		p-value	F-value
	Mean	sd	Mean	sd	Mean	sd		
Imf ₂ ³⁶⁰⁵²	2.81×10^{-4}	2.36×10^{-3}	-5.08×10^{-4}	2.05×10^{-3}	-1.26×10^{-3}	1.68×10^{-3}	0.0000	11.5750
Res ₃ ²⁷⁸⁵⁹	1.25×10^{-5}	2.51×10^{-4}	-1.08×10^{-4}	1.69×10^{-4}	7.74×10^{-5}	2.38×10^{-4}	0.0000	14.4250
Imf ₃ ⁵²⁴⁰⁸	1.52×10^{-4}	7.51×10^{-4}	2.39×10^{-4}	5.78×10^{-4}	-1.82×10^{-4}	7.16×10^{-4}	0.0002	8.6057
Imf ₁ ⁵¹²⁹	1.86×10^{-3}	7.08×10^{-3}	-3.44×10^{-3}	6.14×10^{-3}	-1.47×10^{-4}	7.05×10^{-3}	0.0000	12.1579
Res ₃ ¹⁷⁹²⁶	1.78×10^{-4}	5.25×10^{-4}	-7.67×10^{-5}	4.26×10^{-4}	-4.65×10^{-5}	4.64×10^{-4}	0.0013	6.8268
Imf ₁ ⁶⁷³⁵	-3.34×10^{-4}	9.50×10^{-3}	3.34×10^{-3}	9.40×10^{-3}	-4.79×10^{-3}	1.06×10^{-2}	0.0000	13.8789
Imf ₃ ⁵⁹⁸⁶⁹	-1.60×10^{-4}	6.14×10^{-4}	-1.49×10^{-4}	5.08×10^{-4}	5.92×10^{-5}	5.10×10^{-4}	0.0157	4.2248
Imf ₃ ³⁶²⁶⁹	-1.83×10^{-4}	1.70×10^{-3}	6.83×10^{-4}	1.33×10^{-3}	2.31×10^{-4}	1.65×10^{-3}	0.0031	5.9254
Imf ₃ ³⁵⁵⁷⁹	2.74×10^{-4}	9.00×10^{-4}	2.77×10^{-4}	8.02×10^{-4}	-1.62×10^{-4}	7.88×10^{-4}	0.0006	7.6655
Imf ₁ ⁴¹¹⁰¹	-9.97×10^{-4}	1.00×10^{-2}	-3.89×10^{-3}	9.03×10^{-3}	3.70×10^{-3}	6.93×10^{-3}	0.0000	15.8198
Imf ₂ ¹⁵⁷⁹⁵	-2.31×10^{-3}	5.88×10^{-3}	2.12×10^{-3}	5.96×10^{-3}	-7.01×10^{-5}	7.03×10^{-3}	0.0001	9.5121
Imf ₃ ³⁸³³	4.98×10^{-5}	1.98×10^{-3}	-6.80×10^{-4}	1.58×10^{-3}	8.01×10^{-4}	1.90×10^{-3}	0.0000	13.3147
Imf ₁ ²⁸⁷⁴⁸	4.09×10^{-3}	1.26×10^{-2}	-3.78×10^{-3}	1.24×10^{-2}	-2.93×10^{-3}	1.37×10^{-2}	0.0002	8.7765
Imf ₁ ²³⁵³⁶	1.13×10^{-4}	5.18×10^{-3}	-1.36×10^{-3}	3.96×10^{-3}	2.26×10^{-3}	5.15×10^{-3}	0.0000	11.7654
Res ₃ ⁴²²⁰⁸	-1.42×10^{-5}	2.03×10^{-4}	-8.36×10^{-5}	1.22×10^{-4}	3.22×10^{-5}	1.86×10^{-4}	0.0002	9.0273
Imf ₃ ⁶²⁰⁹⁹	-1.23×10^{-4}	4.79×10^{-4}	1.32×10^{-4}	4.21×10^{-4}	1.69×10^{-4}	5.53×10^{-4}	0.0003	8.3684
Imf ₂ ⁷¹¹⁹	-3.47×10^{-3}	1.47×10^{-2}	6.02×10^{-3}	1.24×10^{-2}	2.62×10^{-3}	1.52×10^{-2}	0.0002	8.9537
Imf ₁ ¹⁴⁴³⁸	9.48×10^{-3}	1.97×10^{-2}	-1.63×10^{-3}	2.03×10^{-2}	-1.20×10^{-2}	1.70×10^{-2}	0.0000	26.0750
Imf ₃ ²¹⁶⁵⁸	-1.55×10^{-4}	7.28×10^{-4}	-2.62×10^{-4}	6.40×10^{-4}	1.96×10^{-4}	7.41×10^{-4}	0.0001	9.4983
Imf ₃ ⁵⁹⁰⁴⁵	4.52×10^{-5}	5.56×10^{-4}	-9.41×10^{-5}	4.19×10^{-4}	-2.48×10^{-4}	4.52×10^{-4}	0.0006	7.6838
Imf ₁ ⁴⁵⁷⁴¹	2.65×10^{-3}	1.25×10^{-2}	-6.57×10^{-3}	8.87×10^{-3}	-2.46×10^{-3}	9.66×10^{-3}	0.0000	15.3110
Imf ₃ ⁴⁶⁵⁵²	-1.65×10^{-5}	6.26×10^{-4}	3.68×10^{-4}	5.04×10^{-4}	-1.50×10^{-4}	5.56×10^{-4}	0.0000	18.2258
Imf ₁ ²³⁷²⁹	3.69×10^{-3}	1.80×10^{-2}	-9.87×10^{-3}	1.46×10^{-2}	3.75×10^{-3}	1.88×10^{-2}	0.0000	16.3404
Imf ₃ ⁴²⁵⁵⁹	1.36×10^{-5}	6.79×10^{-4}	-3.34×10^{-4}	6.02×10^{-4}	1.81×10^{-4}	6.58×10^{-4}	0.0000	13.2290
Imf ₁ ³⁰⁶⁵³	-1.51×10^{-3}	4.74×10^{-3}	1.47×10^{-3}	4.28×10^{-3}	1.16×10^{-3}	5.51×10^{-3}	0.0002	8.8189
Imf ₂ ²⁹¹⁵³	3.70×10^{-4}	3.74×10^{-3}	-4.88×10^{-4}	2.99×10^{-3}	2.34×10^{-3}	3.06×10^{-3}	0.0000	16.1078
Imf ₁ ⁴⁰⁸⁵⁸	-5.70×10^{-4}	1.33×10^{-2}	-2.50×10^{-3}	1.08×10^{-2}	5.94×10^{-3}	1.05×10^{-2}	0.0000	12.0153
Imf ₃ ³⁸⁸⁹²	-7.12×10^{-4}	2.61×10^{-3}	1.63×10^{-3}	2.07×10^{-3}	-1.99×10^{-4}	2.61×10^{-3}	0.0000	19.7658
Imf ₁ ⁴⁶³³	1.54×10^{-4}	7.74×10^{-3}	-1.62×10^{-3}	5.02×10^{-3}	2.83×10^{-3}	6.11×10^{-3}	0.0001	10.0808
Imf ₃ ¹⁷⁸²⁵	5.03×10^{-5}	1.63×10^{-3}	-6.49×10^{-4}	1.12×10^{-3}	2.41×10^{-4}	1.30×10^{-3}	0.0001	9.4572

sd = standard deviation.

References

[1] V. Mitra, J. Metcalf, Functional anatomy and blood supply of the liver, *Anaesth. Intensive Care Med.* 10 (7) (2009) 332–333.

[2] M. Hoffman, Picture of the liver, Retrieved from, <https://www.webmd.com/digestive-disorders/picture-of-the-liver#1>, 2014.

[3] R.L. Siegel, K.D. Miller, A. Jemal, Cancer statistics, 2017, *CA A Cancer J. Clin.* 67 (1) (2017) 7–30.

[4] American Cancer Society, Early detection, diagnosis, and staging, Retrieved from, <https://www.cancer.org/cancer/liver-cancer/detection-diagnosis-staging/detection.html>, 2016.

[5] M.K. Porayko, C. Choudhary, Benign neoplasms of the liver, *Curr. Treat. Options Gastroenterology* 4 (2001) 479–491.

[6] N. Albiin, MRI of focal liver lesions, *Curr. Med. Imaging Rev.* 8 (2) (2012) 107–116.

[7] Mayo Clinic Staff, Liver cancer, obtained from, <https://www.mayoclinic.org/diseases-conditions/liver-cancer/symptoms-causes/dxc-20198168>, 2017.

[8] U.R. Acharya, O. Faust, F. Molinari, S.V. Sree, S.P. Junnarkar, V.K. Sudarshan, Ultrasound-based tissue characterization of fatty liver disease: a screening and diagnostic paradigm, *Knowledge-Based Syst.* 75 (2015) 66–77.

[9] U.R. Acharya, H. Fujita, S. Bhat, U. Raghavendra, A. Gudigar, F. Molinari, A. Vijayanathan, K.H. Ng, Decision support for fatty liver disease using GIST descriptors extracted from ultrasound images, *Inf. Fusion* 29 (2016b) 32–39.

[10] U.R. Acharya, H. Fujita, V.K. Sudarshan, M.R.K. Mookiah, J.E.W. Koh, J.H. Tan, Y. Hagiwara, K.C. Chua, S.P. Junnarkar, A. Vijayanathan, K.H. Ng, An integrated index for identification of fatty liver disease using radon transform and discrete cosine transform features in ultrasound images, *Inf. Fusion* 31 (2016c) 43–53.

[11] U.R. Acharya, U. Raghavendra, H. Fujita, Y. Hagiwara, J.E.W. Koh, J.H. Tan, V.K. Sudarshan, A. Vijayanathan, C.H. Yeong, A. Gudigar, K.H. Ng, Automated characterization of fatty liver disease and cirrhosis using curvelet transform and entropy features extracted from ultrasound images, *Comput. Biol. Med.* 79 (2016a) 250–258.

[12] U.R. Acharya, S.V. Sree, R. Ribeiro, G. Krishnamurthi, R.T. Marinho, J. Sanches, J.S. Suri, Data mining framework for fatty liver disease classification in ultrasound: a hybrid feature extraction paradigm, *Med. Phys.* 39 (7) (2012) 4255–4264.

[13] M. D'Onofrio, S. Crosara, R.D. Robertis, S. Canestrini, R.P. Mucelli, Contrast-enhanced ultrasound of focal liver lesions, *Gastrointest. Imaging* 205 (1) (2015) W56–W66.

[14] J.A. Soye, C.P. Mullan, S. Porter, H. Beattie, A.H. Barltrop, W.M. Nelson, The use of contrast-enhanced ultrasound in the characterization of focal liver lesions, *Ulster Med. J.* 76 (1) (2007) 22–25.

[15] T.V. Bartolotta, A. Taibbi, M. Midiri, R. Lagalla, Focal liver lesions: contrast-enhanced ultrasound, *Abdom. Imaging* 34 (2) (2009) 193–209.

[16] K. Sugimoto, J. Shiraishi, F. Moriyasu, K. Doi, Computer-aided diagnosis for contrast-enhanced ultrasound in liver, *World J. Radiology* 2 (6) (2010) 215–223.

[17] J. Shiraishi, K. Sugimoto, F. Moriyasu, N. Kamiyama, K. Doi, “Computer-aided diagnosis for the classification of focal liver lesions by use of contrast-enhanced ultrasonography”, *Med. Phys.*, vol. 35, no. 5, pp. 1734–1746.

[18] M. D'Onofrio, S. Crosara, R.D. Robertis, S. Canestrini, R.P. Mucelli, Contrast-enhanced ultrasound for focal liver lesions, *Am. J. Radiology* 205 (2015) W56–W66.

[19] D. Mittal, V. Kumar, S.C. Saxena, N. Khandelwal, N. Kalra, Neural network based focal liver lesion diagnosis using ultrasound images, *Comput. Med. Imaging Graph.* 35 (2011) 315–323.

[20] J. Virmani, V. Kumar, N. Kalra, N. Khandelwal, Characterization of primary and secondary malignant liver lesions from B-mode ultrasound, *J. Digital Imaging* 26 (2013) 1058–1070.

[21] J. Virmani, V. Kumar, N. Kalra, N. Khandelwal, PCA-SVM based CAD system for focal liver lesions using B-mode ultrasound images, *Def. Sci. J.* 63 (5) (2013b) 478–486.

[22] J. Virmani, V. Kumar, N. Kalra, N. Khandelwal, Neural network ensemble based CAD system for focal liver lesions from B-mode ultrasound, *J. Digital Imaging* 4 (2014) 520–537.

[23] Y.N. Hwang, J.H. Lee, G.Y. Kim, Y.Y. Jiang, S.M. Kim, Classification of focal liver lesions on ultrasound images by extracting hybrid textural features and using an artificial neural network, *Bio-Medical Mater. Eng.* 26 (2015) S1599–S1611.

[24] N. Manth, J. Virmani, V. Kumar, N. Kalra, N. Khandelwal, Application of texture features for classification of primary benign and primary malignant focal liver lesions, part of the Studies in Computational Intelligence book series, in: *Image Feature Detectors and Descriptors*, vol. 630, 2016, pp. 385–409.

[25] S.M. Pizer, E.P. Amburn, J.D. Austin, R. Cromartie, A. Geselowitz, T. Greer, B.T.H. Romeny, J.B. Zimmerman, K. Zuiderveld, Adaptive histogram equalization and its variations, *Comput. Vis. Graph. Image Process.* 39 (1987) 355–368.

[26] X. Wang, B.S. Wong, T.C. Guan, Image enhancement for radiography inspection, 3rd International Conference on Experimental Mechanics and 3rd International Conference of the Asian Committee on Experimental Mechanics 5852 (2004) 462–468.

[27] J.C. Nunes, S. Guyot, E. Deléchelle, Texture analysis based on local analysis of the bidimensional empirical mode decomposition, *Mach. Vis. Appl.* 16 (2005) 177–188.

[28] N.E. Huang, Z. Shen, S.R. Long, M.C. Wu, H.H. Shih, Q. Zheng, N.C. Yen, C.C. Tung, H.H. Liu, The empirical mode decomposition and the Hilbert spectrum for

- nonlinear and nonstationary time series analysis, in: Proceedings Royal Society London, vol. 454, 1998, pp. 903–995.
- [29] U.R. Acharya, M.R.K. Mookiah, J.E.W. Koh, J.H. Tan, S.V. Bhandary, A.K. Rao, H. Fujita, Y. Hagiwara, K.C. Chua, A. Laude, Automated screening system for retinal health using bi-dimensional empirical mode decomposition and integrated index, *Comput. Biol. Med.* 75 (2016d) 54–62.
- [30] S.S. Dhage, S.S. Hegde, K. Manikantan, S. Ramachandran, DWT-based feature extraction and radon transform based contrast enhancement for improved iris recognition, *Procedia Comput. Sci.* 45 (2015) 256–265.
- [31] U.R. Acharya, M.R.K. Mookiah, J.E.W. Koh, J.H. Tan, S.V. Bhandary, A.K. Rao, Y. Hagiwara, K.C. Chua, A. Laude, Automated diabetic macular edema (DME) grading system using DWT, DCT features and maculopathy index, *Comput. Biol. Med.* 84 (2017) 59–68.
- [32] A. Gun, M. Gupta, B. Dasgupta, *Fundamentals of Statistics*, fourth ed., The World Press Private Ltd, Kolkata, India, 2008.
- [33] H. He, Y. Bai, E.A. Garcia, S. Li, ADASYN: adaptive synthetic sampling approach for imbalanced learning, in: *IEEE International Joint Conference on Neural Networks*, Hong Kong, China, 2008, pp. 1322–1328.
- [34] J. Kennedy, R. Eberhart, Particle swarm optimization, in: *Proceedings of the IEEE International Conference on Neural Network*, Perth, Western Australia, 1995, pp. 1942–1948.
- [35] D.F. Specht, Probabilistic neural networks for classification, mapping, or associative memory, *IEEE International Conference on Neural Networks I* (1998) 525–532.
- [36] C. Cortes, V. Vapnik, Support vector networks, *Mach. Learn.* 20 (1995) 273–297.
- [37] A. Khan, H. Farooq, Principal component analysis-linear discriminant analysis feature extractor for pattern recognition, *Int. J. Comput. Sci.* 8 (2011) 267–270.
- [38] T.M. Cover, P.E. Hart, Nearest neighbor pattern classification, *IEEE Trans. Inf. Theory* 13 (1) (1967) 21–27.
- [39] T.K. Ho, The random subspace method for constructing decision forests, *IEEE Trans. Pattern Analysis Mach. Intell.* 20 (8) (1998) 832–844.
- [40] R.O. Duda, P.E. Hart, D.G. Stork, *Pattern Classification*, second ed., John Wiley and Sons, New York, 2001.
- [41] J.H. Tan, U.R. Acharya, S.V. Bhandary, K.C. Chua, S. Sivaprasad, Segmentation of optic disc, fovea and retinal vasculature using a single convolutional neural network, *J. Comput. Sci.* 20 (2017a) 70–79.
- [42] J.H. Tan, H. Fujita, S. Sivaprasad, S.V. Bhandary, A.K. Rao, K.C. Chua, U.R. Acharya, Automated segmentation of exudates, haemorrhages, microaneurysms using single convolutional neural network, *Inf. Sci.* 426 (2017b) 66–76.